Targeting kidney mesangium by nanoparticles of defined size

Chung Hang J. Choi[a], Jonathan E. Zuckerman[a], Paul Webster[b], and Mark E. Davis[a,1]

[a]Chemical Engineering, California Institute of Technology, Pasadena, CA 91125; and [b]Ahmanson Electron Microscopy Advanced Imaging Center, House Ear Institute, Los Angeles, CA 90057

Contributed by Mark E. Davis, March 7, 2011 (sent for review February 8, 2011)

Nanoparticles are being investigated for numerous medical applications and are showing potential as an emerging class of carriers for drug delivery. Investigations on how the physicochemical properties (e.g., size, surface charge, shape, and density of targeting ligands) of nanoparticles enable their ability to overcome biological barriers and reach designated cellular destinations in sufficient amounts to elicit biological efficacy are of interest. Despite proven success in nanoparticle accumulation at cellular locations and occurrence of downstream therapeutic effects (e.g., target gene inhibition) in a selected few organs such as tumor and liver, reports on effective delivery of engineered nanoparticles to other organs still remain scarce. Here, we show that nanoparticles of ∼75 ± 25-nm diameters target the mesangium of the kidney. These data show the effects of particle diameter on targeting the mesangium of the kidney. Because many diseases originate from this area of the kidney, our findings establish design criteria for constructing nanoparticle-based therapeutics for targeting diseases that involve the mesangium of the kidney.

gold nanoparticles | kidney targeting | mesangial cells | particle size

Constructing nanoparticles for drug delivery requires knowledge in colloidal science and biology, where biological constraints generally dictate the design of nanoparticle therapeutics and imaging agents (1–4). A celebrated design criterion is the notion of renal clearance (5, 6). That is, nanoparticles will experience rapid clearance by the kidney if they are smaller than ∼10 nm in diameter. Such clearance originates from the innate function of the kidney as a blood filter.

The structural and functional unit of the kidney, the nephron, consists of the renal corpuscle and tubule system. The renal corpuscle contains a tuft of blood capillaries and support tissue (the mesangium) (Fig. S1) called the glomerulus. A fraction of blood plasma entering the glomerulus will pass through the glomerular filtration apparatus to produce an ultrafiltrate, which will be collected by the tubule system and ultimately, processed into urine. The first component is the glomerular endothelium, with pores that have been reported to be in the range of 80–100 nm in diameter (7). Next, the glomerular basement membrane (GBM), a 300- to 350-nm-thick basal lamina rich in heparan sulfate (8) and charged proteoglycans with an average pore size of 3 nm (9), filters small molecules by size and charge. Behind the GBM lies podocytes, cells with interdigitating foot processes that form filtration slits that are 32 nm wide (10). The glomerular filtration apparatus, taken in its entirety, possesses an effective size cutoff of 10 nm, and it is responsible for the rapid renal clearance of small nanoparticles. Many nanoparticle-based contrasting agents for in vivo imaging were designed to be smaller than this size cutoff (11, 12). Prolonged residency of nanoparticles in the kidney has been shown to induce toxicity in the form of cell shrinkage because of excessive nanoparticle uptake by renal cells (13, 14). Closer examination of the renal corpuscle reveals the existence of another intriguing size cutoff that would affect the distribution pattern. Within the renal corpuscle, in the absence of GBM and podocytes, the sole dividing barrier between the mesangium (mesangial cells and extracellular matrix) and the glomerulus is the fenestrated endothelium. Submicron-sized nanoparticles may feasibly diffuse and accumulate indefinitely in the mesangium after they depart from the glomerulus through these pores. Here, we illustrate the size-dependent delivery of PEGylated gold nanoparticles to the kidney mesangium.

Results and Discussion

Assembly of Au_x-PEG_y Nanoparticles. Gold-based nanoparticles (AuNPs) were used here for the following reasons. They are compatible with multiple imaging methods. As rigid and nondecomposable objects, submicron-sized AuNPs larger than ∼10 nm cannot escape the kidney by renal clearance. Unmodified gold nanoparticles of different sizes have ζ-potentials ranging from −19 to −28 mV. The measured ζ-values are consistent with predictions using classical electrokinetic theory (Fig. S2), and they suggest that unmodified AuNPs of all sizes share the same surface charge density (σ). Next, to create particles of the same surface charge, we exploit the charge screening effect of PEG. The larger that the gold particles are, the more negative that the surface charge is. Thus, creating a set of nanoparticles with variable size and relatively constant surface charge would require the engraftment of longer PEG chains onto the larger nanoparticles. This concept prompted us to use an assortment of PEGylated Au_x-PEG_y NPs possessing gold particles of different core diameters (x) and PEGs of different chain lengths (y) (Table 1). The engraftment procedure entailed the use of methoxy-PEG-thiol (mPEG-SH) molecules, whose terminal thiol groups can react with the gold surface through the formation of gold-thiol covalent bonds. Careful choice of x and y gave rise to a near-constant ζ (roughly −10 mV) for Au_x-PEG_y NPs of various final hydrodynamic sizes (Table 1). In general, the engraftment of each additional 2,000 molecular weight of PEG onto the gold surface translates to an increase of 5 nm in the hydrodynamic diameter of Au_x-PEG_y NPs. This approximate linearity between the PEG corona thickness and chain length is consistent with previous predictions for tethered polymer brushes on spherical interfaces without pronounced curvature (15) (Tables S1 and S2). All Au_x-PEG_y NPs showed stability in salt solution after 24 h, with hydrodynamic sizes in PBS roughly equal to those in water (Table 1).

Blood Pharmacokinetics. BALB/c mice (n = 3) received single i.v. injections of each type of Au_x-PEG_y NP at the same particle concentration. From each mouse, blood was withdrawn through the saphenous vein at various time points to evaluate for gold content using inductively coupled plasma MS (ICP-MS). With extensive surface engraftment of PEG ($y \geq 4{,}000$), all particles manifested extended blood circulation, with a half-life ($t_{1/2}$) that

Author contributions: C.H.J.C. and M.E.D. designed research; C.H.J.C. and J.E.Z. performed research; C.H.J.C., J.E.Z., P.W., and M.E.D. analyzed data; and C.H.J.C. and M.E.D. wrote the paper.

The authors declare no conflict of interest.

Freely available online through the PNAS open access option.

[1]To whom correspondence should be addressed. E-mail: mdavis@cheme.caltech.edu.

This article contains supporting information online at www.pnas.org/lookup/suppl/doi:10.1073/pnas.1103573108/-/DCSupplemental.

Table 1. Physicochemical properties and in vivo characteristics of Au_x-PEG_y NPs

NP	Core (x; in nm)	PEG (y; in Da)	HD water (nm)	HD 1× PBS (nm)	ZP (mV)	$t_{1/2}$ (h)	Ω (% ID)	GTE (%)	SI
Au_5-$PEG_{5,000}$	5.3 ± 0.5	5,000	26.2 ± 0.3	24.8 ± 0.5	−8.44 ± 0.85	48.9	0.2 ± 0.1	0	0
Au_{20}-$PEG_{5,000}$	21.6 ± 0.2	5,000	43.1 ± 0.2	41.4 ± 0.2	−9.62 ± 0.62	31.8	1.2 ± 0.5	50	+
Au_{40}-$PEG_{4,000}$	41.2 ± 0.2	4,130	59.1 ± 0.3	58.6 ± 0.5	−12.34 ± 1.21	13.8	3.0 ± 0.6	80	++
Au_{50}-$PEG_{5,000}$	51.4 ± 0.2	5,000	78.8 ± 0.2	76.5 ± 0.4	−10.91 ± 1.33	13.7	4.6 ± 0.9	100	+++
Au_{60}-$PEG_{7,000}$	58.1 ± 0.5	7,359	94.6 ± 0.5	96.2 ± 0.2	−12.51 ± 1.24	11.4	1.9 ± 0.4	90	+++
Au_{80}-$PEG_{10,000}$	76.5 ± 0.3	10,000	127.6 ± 2.1	128.9 ± 0.9	−8.93 ± 0.67	8.7	0.7 ± 0.4	70	++
Au_{100}-$PEG_{20,000}$	98.3 ± 0.3	20,000	167.4 ± 9.6	164.3 ± 8.6	−9.76 ± 0.31	6.8	0.5 ± 0.3	60	+

GTE, glomerular targeting efficiency; HD, hydrodynamic diameter; $t_{1/2}$, blood half-life; x, core diameter of AuNP; y, chain length of grafted PEG; SI, staining index (an arbitrary score that ranks both the intensity and spread of the silver stain, where +++ and 0 are the maximum and minimum values, respectively); ZP, ζ-potential in 1 mM KCl; Ω, kidney bulk particle content. The table presents in vitro data as average ± SD from triplicates of experiments as well as in vivo data as average ± SD from three animals per particle type.

spans from 7 to 38 h. Particle size and $t_{1/2}$ were inversely correlated (Fig. 1*A* and Table S3). The simultaneous increase in x and y led to reduction in $t_{1/2}$, indicating that size-dependent internal clearance, not colloidal stability conferred by PEGylation, played a dominant role in determining particle blood circulation.

Organ-Level Distribution. Mice were then euthanized 24 h after injection to extract organs for detection of bulk gold content using ICP-MS. For all particle sizes, gold content of the six organs plus the blood samples collected at three time points summed up to ≥70% injected dose (ID), thus constituting a mass balance that accounts for the destinations of most injected Au_x-PEG_y NPs. Overall, the liver, spleen, and kidney were the main sites of particle accumulation, whereas the lung, pancreas, and heart showed negligible (<0.5% ID) particle retention (Fig. 1*B* and Table S4). At 24 h after dosing, the liver and spleen both showed a positive correlation between particle size and degree of particle uptake, which is in agreement with previous reports that the degree of particle phagocytosis by Kupffer cells and spleen macrophages is largely size-dependent [the larger the nanoparticles, the greater the uptake in the reticuloendothelial system (RES)] (16). From Fig. 1, the blood nanoparticle content at 24 h seems to correlate with uptake by the RES (increased uptake by the RES is accompanied by lower content in the blood, leading to shorter circulation half-life). Lastly and most importantly, the kidney revealed an unexpected size-dependent nanoparticle retention pattern; there exists a particle size (Au_{50}-$PEG_{5,000}$) at which renal accumulation is maximal.

Tissue-Level Renal Distribution. To understand the size-dependent accumulation in the kidney, we prepared silver-enhanced kidney sections to reveal the distribution of Au_x-PEG_y NPs at the tissue level. Gold selectively catalyzes the reduction of silver ions and deposition of metallic silver, making nano-sized objects embedded in kidney sections visible under light microscopy. Within the cortex, most particles resided either near resident phagocytes

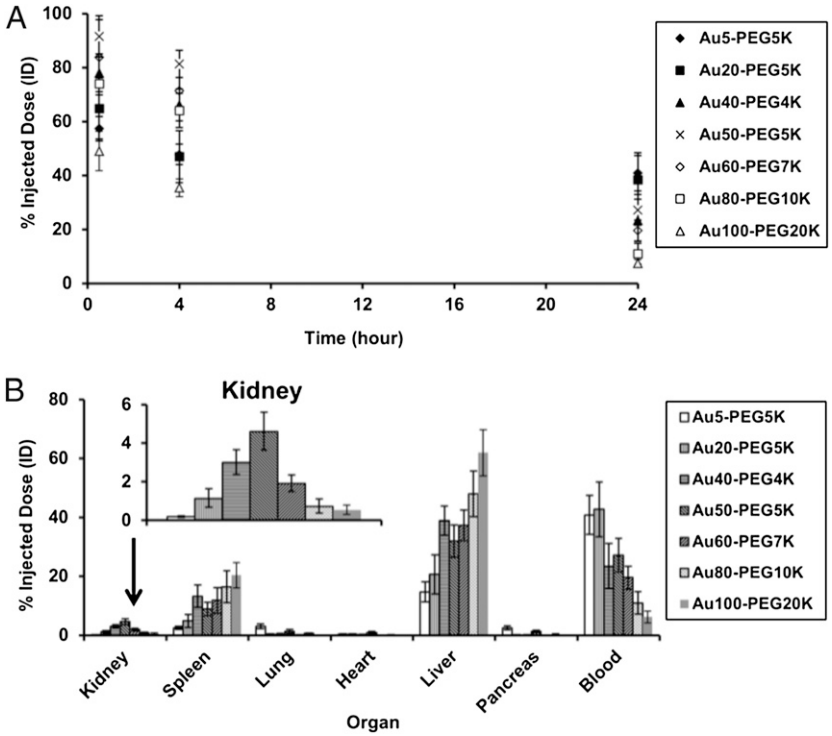

Fig. 1. (*A*) Blood pharmacokinetics. All Au_x-PEG_y NPs showed revealed extended circulation times in blood. (*B*) Organ-level biodistribution. Bulk particle localization in the liver, spleen, and kidney was size-dependent. Gold contents are normalized to percent injected dose (% ID). For all particle sizes, the five named organs plus the blood compartment accounted for at least 70% ID of the injected dose. Error bars indicate 1 SD from each Au_x-PEG_y NP class (n = 3).

within peritubular capillaries, which intertwine the cortical tubules (proximal convoluted tubules and distal convoluted tubules), or inside renal corpuscles.

Particle accumulation at peritubular capillaries did not show clear correlation with size (Fig. S3). However, particle accumulation inside renal corpuscles reveals a strong function of size (Fig. 2). The smallest particles (Au_5-$PEG_{5,000}$) were virtually undetectable in the renal corpuscles but were found in peritubular capillaries (Fig. S4*A*). Au_{20}-$PEG_{5,000}$ nanoparticles accumulated in the renal corpuscles and rarely accumulated in the peritubular capillaries. Only ~50% of the renal corpuscles contained Au_{20}-$PEG_{5,000}$ NPs, and the staining scattered all over the extracellular space (mesangium) outside the mesangial cells. The staining intensity seemed mild (Fig. 2*A*). For Au_{40}-$PEG_{4,000}$ NPs, particle staining within the renal corpuscles became more intense; ~80% of the renal corpuscles were stained positive for particles, and staining localized closer to mesangial cells (Fig. S4*B*).

Similar accumulation patterns were apparent for Au_{50}-$PEG_{5,000}$ NPs, except that 100% of the renal corpuscles examined under the light microscope were stained positive for particles. Closer inspection of each renal corpuscle revealed that the most intense silver is adjacent to mesangial cells throughout the largest area fraction of the renal corpuscles among all particle sizes (Fig. 2*B*). Incidentally, this complete glomerular targeting efficiency (GTE) matches strongly with the maximal bulk particle content in the kidney observed for Au_{50}-$PEG_{5,000}$ NPs. The GTE

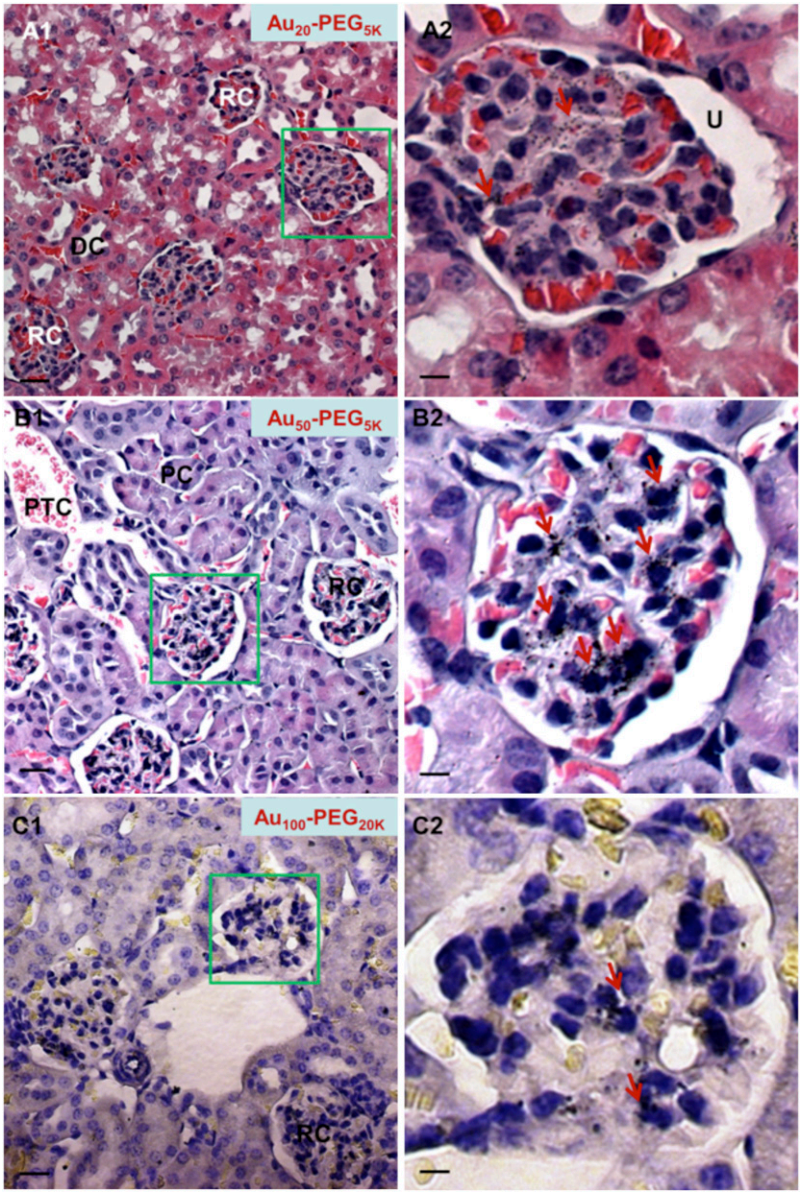

Fig. 2. Tissue-level distribution in renal corpuscles within the cortex. Representative light micrographs of silver-enhanced kidney sections show the extent of glomerular targeting by particles. Au_x-PEG_y NPs accumulated in a size-dependent manner. (*A*) Au_{20}-$PEG_{5,000}$ NPs were detectable in small quantities within renal corpuscles. (*B*) Au_{50}-$PEG_{5,000}$ NPs displayed the most intense staining in the largest area of renal corpuscles among all particle sizes. Silver staining (dark specks indicated by red arrows) was present in every single renal corpuscle observed under the light microscope, resulting in complete glomerular targeting efficiency (GTE). (*C*) Au_{100}-$PEG_{20,000}$ NPs only accumulated in the renal corpuscles in minute amounts, presumably because of their inability to penetrate through the fenestrated glomerular endothelium. *Right* illustrates the magnified renal corpuscle (green box) shown in *Left*. (Scale bar: *Left*, 10 μm; *Right*, 3 μm.) DC, distal convoluted tubule; PC, proximal convoluted tubule; PTC, peritubular capillaries; RC, renal corpuscle; U, urinary space.

for Au_{60}-$PEG_{7,000}$ NPs was also close to complete (~90%), and such particles also elicited very intense silver staining near the mesangial cells (Fig. S4*C*).

Finally, Au_{80}-$PEG_{10,000}$ and Au_{100}-$PEG_{20,000}$ NPs gave a GTE of 60–70%. Because of the catalytic nature of staining, larger Au_x-PEG_y NPs are expected to produce more silver deposition on their periphery. Although silver staining can confirm the presence of Au_x-PEG_y NPs, the intensity alone does not provide the quantitation of actual particle content. Thus, besides the absolute magnitude of intensity, the spread of staining (areal fraction covered by silver) within renal corpuscles is also an important measure. We report in Table 1 what we denote as the staining index (SI), an arbitrary measure that accounts for both intensity and spread of staining. For the highest score (i.e., +++), particles (like Au_{50}-$PEG_{5,000}$ NPs) accumulated in the highest areal fraction of the renal corpuscles and also, accumulated at the highest intensity. Typically, the same particles can achieve a high GTE, meaning that they can be found frequently in different renal corpuscles throughout the cortex. For the lowest score (i.e., 0), particles (like Au_5-$PEG_{5,000}$ NPs) resided in limited areas of the renal corpuscles and usually, resided at undetectable densities. Typically, the same particles can achieve a low GTE, implying their low occurrence in different renal corpuscles throughout the cortex.

For Au_{80}-$PEG_{10,000}$ NPs, silver staining was found in limited regions of renal corpuscles, despite their intense staining, yielding an SI score of ++. The largest particles, Au_{100}-$PEG_{20,000}$ NPs, barely occupied a sizeable areal fraction of the renal corpuscles and showed very modest staining, leading to their score of + for the SI. Overall, the SI of the largest nanoparticles

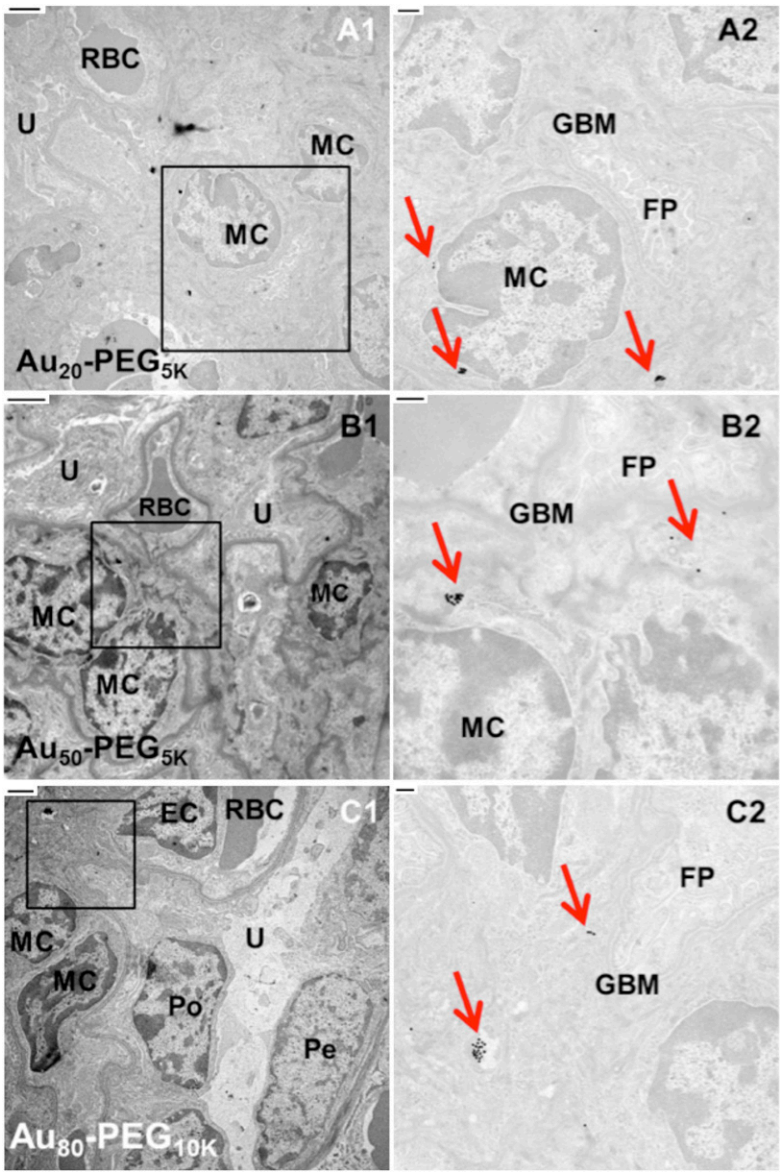

Fig. 3. Cellular-level distribution in renal corpuscles within the cortex. Representative transmission electron micrographs show particle accumulation in the mesangium (mesangial cells and extracellular matrix). *Right* illustrates the magnified portion (black box) shown in *Left*. (Scale bar: *Left*, 2 μm; *Right*, 500 nm.) Red arrows in *Right* indicate clusters of Au_x-PEG_y NPs. (*A*) A small portion of Au_{20}-$PEG_{5,000}$ NPs localized in mesangial cells within the renal corpuscles. (*B*) Au_{50}-$PEG_{5,000}$ NPs experienced the most prominent uptake by mesangial cells among all particle sizes. (*C*) Au_{80}-$PEG_{10,000}$ NPs deposited in the mesangium in drastically reduced amounts. EC, endothelial cell; FP, foot processes of podocytes; GBM, glomerular basement membrane; MC, mesangial cell; PC, proximal convoluted tubule; Pe, parietal layer of Bowman's capsule; Po, podocyte; RBC, red blood cell; U, urinary space.

(Au_{80}-$PEG_{10,000}$ and Au_{100}-$PEG_{20,000}$ NPs) was lower than that of Au_{50}-$PEG_{5,000}$ NPs. Taken together, Au_{80}-$PEG_{10,000}$ and Au_{100}-$PEG_{20,000}$ NPs target 60–70% of the renal corpuscles and within each corpuscle, target a very limited area fraction and moderately intense staining.

The histological data collectively suggest a size-dependent localization of Au_x-PEG_y NPs within renal corpuscles in the kidney cortex. Because such particles do not have a constant PEG chain length, one may question whether the distribution of nanoparticles in renal corpuscles is PEG-dependent. To address this point, we investigated the tissue-level in vivo distribution of Au_{80}-$PEG_{5,000}$ NPs (hydrodynamic size = 97.1 ± 1.9 nm; ζ-potential = −16.77 ± 1.14 mV) in renal corpuscles, noting that such particles possess a very similar hydrodynamic size and ζ-potential of Au_{60}-$PEG_{7,000}$ NPs. Histological analysis reveals accumulation of Au_{80}-$PEG_{5,000}$ NPs in the renal corpuscles in similar intensity and area as that of Au_{60}-$PEG_{7,000}$ NPs but not Au_{80}-$PEG_{10,000}$ NPs, supporting the suggestion that the distribution of nanoparticles in renal corpuscles is size-dependent.

Cellular-Level Renal Distribution. Transmission electron microscopy (TEM) was used to determine the intracellular localization patterns of the nanoparticles residing in the renal cortex. In agreement with the histological data, particles of all sizes were either engulfed by resident phagocytes or remained as isolated entities in circulation inside pertitubular blood capillaries. Particle accumulation in peritubular blood capillaries was not size-dependent (Fig. S5). Retention of particles in renal corpuscles, however, is a strong function of size (Fig. 3). Smaller particles (Au_{20}-$PEG_{5,000}$ NPs) entered the mesangium within renal corpuscles in minute quantities (Fig. 3*A*). As size increases, Au_x-PEG_y NPs showed more association with mesangial cells. Au_{50}-$PEG_{5,000}$ NPs accumulated in multiple clusters either within mesangial cells or in the extracellular matrix outside mesangial cells. The clustering density was the most pronounced among all particle sizes, consistent with the histological data (Fig. 3*B*). Particles of similar sizes (Au_{40}-$PEG_{4,000}$ and Au_{60}-$PEG_{7,000}$ NPs) also showed appreciable particle accumulation in the mesangium (Fig. S6). Larger particles (Au_{80}-$PEG_{10,000}$ NPs) only resided at the extracellular space in isolated amounts (Fig. 3*C*). The TEM data reveal a size at which particle association with mesangial cells was maximal (Au_{50}-$PEG_{5,000}$ NPs). This particular size maximized bulk kidney particle content and glomerular targeting. Thus, Au_{50}-$PEG_{5,000}$ represents the particle size that maximizes kidney targeting at the organ, tissue, and cellular (mesangium) levels.

The average pore diameter of the fenestrated glomerular endothelia is reported to be 80–100 nm, roughly the hydrodynamic size of Au_{50}-$PEG_{5,000}$ and Au_{60}-$PEG_{7,000}$ NPs. Particles larger than this size cutoff (Au_{80}-$PEG_{10,000}$ and Au_{100}-$PEG_{20,000}$ NPs) may experience steric hindrance when permeating through the pores to enter the mesangium and access the mesangial cells. On the contrary, smaller particles (Au_{20}-$PEG_{5,000}$ and Au_{40}-$PEG_{4,000}$ NPs) are freely accessible to the mesangium. Thus, the size exclusion effect may account for the lower kidney particle content and weaker glomerular targeting of the largest particles. From TEM data, size-dependent uptake occurs solely at mesangial cells, which come in two types. The first type is contractile mesangial cells, which resemble vascular smooth muscle cells and fibroblasts that regulate surface area for glomerular filtration of fluids and mesangial volume. The second type involves mononuclear resident phagocytes derived from the bone marrow (17). From the ICP-MS data, particle uptake by spleen macrophages and hepatic Kupffer cells (both of bone marrow origin) increases with increasing particle size. Below the size cutoff in kidney, larger particles (Au_{50}-$PEG_{5,000}$ NPs) can penetrate through the endothelial pores, enter the mesangium, and accumulate inside mesangial cells (likely, the phagocytic-type mesangial cells). The smallest particles (Au_5-$PEG_{5,000}$ NPs) may transiently enter the mesangium but may not favor prolonged retention because of lack of phagocytosis by mesangial cells. The absence of a cellular sink may lead to their low bulk particle content.

This work systematically examines the distribution of 10- to 150-nm nanoparticles in the kidney from a systemic injection. From measuring blood pharmacokinetics as well as distribution patterns at the organ, tissue, and cellular levels, the results suggest that there is an optimal size range (e.g., Au_{50}-$PEG_{5,000}$ NPs) that maximizes bulk particle uptake in the kidney, deposition of particles in renal corpuscles within the cortex, and uptake of particles by mesangial cells within renal corpuscles. When using nanoparticles as cancer therapeutics, accumulations in single-digit percent ID amounts in the tumor can lead to gene inhibition and tumor reduction (18). Thus, the accumulation of Au_x-PEG_y NPs (1–5% ID) in the kidney at these amounts may be able to impart efficacy with kidney diseases. Moreover, the lack of significant localization (0.7% ID) of larger particles (Au_{80}-$PEG_{10,000}$ NPs; ∼130 nm in diameter) provides an in vivo calibration to the size of the glomerular endothelial pores. Most reported values for this pore size are derived from direct measurements of TEM and scanning electron microscopy (SEM) images. Sample processing for microscopy involves repeated dehydration and may lead to shrinkage of fine cellular features. The pore size reported here (130 nm) depicts the glomerular endothelial morphology at physiologically relevant conditions.

Materials and Methods

General. Unless otherwise mentioned, all PEG raw materials were purchased from Laysan Bio. All organic solvents were purchased from Sigma. PBS is comprised of 150 mM NaCl and 50 mM sodium phosphate (pH 7.4).

Synthesis of $mPEG_{4,000}$-SH and $mPEG_{7,000}$-SH. Fifty milligrams amine-$PEG_{3,400}$-thiol (14.7 μmol) were reacted with 40.4 mg methoxy-PEG_{550}-(succinimidyl propionate) (73.5 μmol) in 50 μL triethylamine (TEA) and 1.2 mL anhydrous dichloromethane (DCM). The reaction proceeded at room temperature (RT), with stirring for 7 h. The crude mixture was dried under vacuum and dialyzed against deionized water using a 3-kDa Amicon MWCO membrane (Millipore); 15 mg amine-$PEG_{5,000}$-thiol (3.0 μmol) was reacted with 60 mg methoxy-$PEG_{2,000}$-(succinimidyl valerate) (30.0 μmol) in 50 μL TEA and 1.2 mL anhydrous DCM. The reaction proceeded at RT, with stirring for 16 h. The crude mixture was dried under vacuum and dialyzed against deionized water using a 30-kDa Amicon MWCO membrane (Millipore). The correct fraction (7,000 Da) was separated with HPLC using a TSK gel G3000SW column (Tosoh Bioscience). Final molecular weights were confirmed by MALDI-TOF.

Assembly of Au_x-PEG_y NPs. Methoxy-PEG-thiol (purchased or synthesized above) of a particular molecular weight (y = 4,000, 5,000, 7,000, 10,000, and 20,000) and dissolved in deionized water was added to 3 mL aqueous suspension of unconjugated gold colloids (Ted Pella) of a designated core size (x = 5, 20, 40, 50, 60, 80, and 100 nm) at an excess concentration of ∼9 PEG strands per nm^2 gold surface [e.g., to ensure complete coverage, PEGylation of 50 nm AuNPs required the addition of 10 μL 1 mM $mPEG_{5,000}$-thiol (in deionized water) to 0.5 mL aqueous suspension of 2.25×10^{10} particles]. All PEGylation reactions proceeded at room temperature for 2 h with constant stirring. To remove any unbound methoxy-PEG-thiol, the reaction mixture was dialyzed against deionized water using a 30- or 100-kDa Amicon MWCO membrane (Millipore) three times.

Physicochemical Characterization of Au_x-PEG_y NPs. Hydrodynamic diameter (HD) and ζ-potential (ZP) of Au_x-PEG_y NPs were measured using ZetaPals (Brookhaven). For HD measurements, the particle pellet was resuspended in 1.2 mL deionized water or PBS. Reported HDs are average values from three runs of 3 min each. For ZP analysis, the pellet was resuspended in 1.4 mL 1 mM KCl. Reported ZPs are average values from 10 runs each, with a target residual of 0.012 measured at a conductance of 320 ± 32 μS.

Animal Experiments. For each type of Au_x-PEG_y NPs, three 9-wk-old female BALB/c mice (Jackson Laboratory) received i.v. injections of particles through the tail vein at a concentration of 4.5×10^{11} particles/mL formulated in 120 μL filtered 5% glucose in deionized water (D5W). At three consecutive time points after injection (30 min, 4 h, and 24 h), 30 μL mouse blood were drawn from each mouse through its saphenous vein using Microvette CB 300 Capil-

lary Blood Collection Tubes with EDTA (Sarstedt). Blood samples were stored at 4 °C for future use. After 24 h, mice were euthanized by CO_2 overdose for the collection of the liver, kidney, lung, heart, spleen, and pancreas. All organs were fixed in 4% paraformaldehyde (PFA) in PBS for 3 d.

ICP-MS. Homogenized organs were oxidized in 0.5 mL acid mixture (70% HNO_3 and 35% HCl at a 3:1 volume ratio) in a microwave until they were fully dissolved. After adding 20.5 mL deionized water, the sample was centrifuged at 3,200 × *g* for 15 min to remove cell debris, leaving the supernatant for gold content analysis using HP 4500 ICP-MS (Agilent). Nebulization occurred with a flow of 1.3 L/min argon using a Babbington-type nebulizer in a Pyrex Scott-type spray chamber. The argon plasma power was 1,200 W, with a flow of 15 L/min and an auxiliary flow of 1.1 L/min. A calibration curve against known concentrations of Au_x-PEG_y NPs of all sizes was used to measure the gold content, using 2.5% HNO_3 and 0.42% HCl as the blank solvent and tissues from uninjected BALB/c mice to account for background organ gold content. Reported values are expressed as percent ID. Error bars indicate 1 SD in each mouse group (n = 3). Each mouse weighed ~20 g at the time of experiment and had a total blood volume of 1.6 mL (average mouse volume is 77–80 μL/g).

Histology with Silver Enhancement. PFA-fixed organs were dehydrated and embedded in molten paraffin to generate sections that were 4-μm thick. Sections were deparrafinized with xylene, rehydrated with a reducing ethanol gradient, rinsed with deionized water extensively, dried, and stained for Au_x-PEG_y NPs using the Silver Enhancement Kit for Light and Electron Microscopy (Ted Pella) in the dark for 20 min at RT. After rinsing with running tap water for 2 min to remove excess silver, sections were counterstained with Gill's 3 hematoxylin and 1% eosin (in 95% ethanol) for 40 s each and then mounted with Permount for viewing under an Axioplan 2 light microscope (Zeiss) with a 40× objective. To estimate the GTE of particles to renal corpuscles from light micrographs, 300 renal corpuscles, selected at random positions from 10 to 15 kidney sections per injected mouse, were inspected visually for the presence of silver stains. For SI, both the staining intensity and spread of these 300 renal corpuscles were scored.

TEM. Tissue blocks (~1 mm^3) were fixed in 2.5% glutaraldehyde (in 0.1 M sodium cacodylate, pH 7.4) for 2 h, stained by 1% OsO_4 at 4 °C for 2 h, and stained by 0.9% OsO_4 and 0.3% $K_3Fe(CN)_6$ at 4 °C for 2 h. Gradual dehydration with ethanol and propylene oxide enabled tissue embedding in Epon 812 resins (Electron Microscopy Sciences); 80-nm-thick sections were deposited on carbon- and formvar-coated 200-mesh nickel grids (EMS) and stained with 3% uranyl acetate and Reynolds lead citrate for visualization under a 120-kV BioTwin CM120 TEM (Philips).

ACKNOWLEDGMENTS. We thank Debbie Guerrero and Siva Wu from the House Ear Institute for advice in histology. This work was supported by National Cancer Institute Grant CA119347 and National Institutes of Health Grant NIH 2P30DC006272-06 and the Ahmanson Foundation.

1. Davis ME, Chen ZG, Shin DM (2008) Nanoparticle therapeutics: An emerging treatment modality for cancer. *Nat Rev Drug Discov* 7:771–782.
2. Peer D, et al. (2007) Nanocarriers as an emerging platform for cancer therapy. *Nat Nanotechnol* 2:751–760.
3. Davis ME (2009) The first targeted delivery of siRNA in humans via a self-assembling, cyclodextrin polymer-based nanoparticle: From concept to clinic. *Mol Pharm* 6:659–668.
4. Zimmermann TS, et al. (2006) RNAi-mediated gene silencing in non-human primates. *Nature* 441:111–114.
5. Choi HS, et al. (2007) Renal clearance of quantum dots. *Nat Biotechnol* 25:1165–1170.
6. Choi HS, et al. (2009) Tissue- and organ-selective biodistribution of NIR fluorescent quantum dots. *Nano Lett* 9:2354–2359.
7. Luft FC, et al. (1982) Effects of moxalactam and cefotaxime on rabbit renal tissue. *Antimicrob Agents Chemother* 21:830–835.
8. Kanwar YS, Farquhar MG (1979) Presence of heparan sulfate in the glomerular basement membrane. *Proc Natl Acad Sci USA* 76:1303–1307.
9. Ogawa S, et al. (1999) High-resolution ultrastructural comparison of renal glomerular and tubular basement membranes. *Am J Nephrol* 19:686–693.
10. Lahdenkari A-T, et al. (2004) Podocytes are firmly attached to glomerular basement membrane in kidneys with heavy proteinuria. *J Am Soc Nephrol* 15:2611–2618.
11. Tan M, et al. (2010) An effective targeted nanoglobular manganese(II) chelate conjugate for magnetic resonance molecular imaging of tumor extracellular matrix. *Mol Pharm* 7:936–943.
12. Schipper ML, et al. (2009) Particle size, surface coating, and PEGylation influence the biodistribution of quantum dots in living mice. *Small* 5:126–134.
13. L'Azou B, et al. (2008) In vitro effects of nanoparticles on renal cells. *Part Fibre Toxicol* 5:1–14.
14. Chen Z, et al. (2006) Acute toxicological effects of copper nanoparticles in vivo. *Toxicol Lett* 163:109–120.
15. Dan N, Tirrell M (1992) Polymers tethered to curved interfaces. A self-consistent-field analysis. *Macromolecules* 25:2890–2895.
16. Sadauskas E, et al. (2007) Kupffer cells are central in the removal of nanoparticles from the organism. *Part Fibre Toxicol* 4:1–7.
17. Schreiner GF (1992) The mesangial phagocyte and its regulation of contractile cell biology. *J Am Soc Nephrol* 2:S74–S82.
18. Bartlett DW, Su H, Hildebrandt IJ, Weber WA, Davis ME (2007) Impact of tumor-specific targeting on the biodistribution and efficacy of siRNA nanoparticles measured by multimodality in vivo imaging. *Proc Natl Acad Sci USA* 104:15549–15554.